Internal solitary waves in the Coastal Mixing and Optics 1996 experiment: Multimodal structure and resuspension

D. J. Bogucki
Rosenstiel School of Marine and Atmospheric Science, University of Miami, Miami, Florida, USA

L. G. Redekopp
Department of Aerospace and Mechanical Engineering, University of Southern California, Los Angeles, California, USA

J. Barth
College of Oceanic and Atmospheric Sciences, Oregon State University, Corvallis, Oregon, USA

Received 16 December 2003; revised 8 November 2004; accepted 19 January 2005; published 26 February 2005.

[1] Observations of internal solitary waves (ISWs) and of their role in sediment resuspension during the Coastal Mixing and Optics 1996 (CMO 96) experiment are reported. The largest resuspension events observed in the experiment can be related to retarded flow under the wave footprint. Two distinctly different periods of resuspension events could be distinguished based on the prevailing atmospheric conditions: a calm period, which we consider characteristic of nominal conditions, and an energetic period, during which two major storms occurred. ISWs arrived at the mooring site from a variety of sources, though a common intermodal dynamics seemed to occur repeatedly. Both mode 1 and mode 2 ISWs have been observed. The present analysis of the month-long portion of the CMO 96 data set constitutes the first reported observations, insofar as we are aware, of mode 2 waves on the continental shelf. Both mode 1 and mode 2 ISWs were found to stimulate resuspension. The mode 2 waves seem to be generated locally by resonant or topographic interactions with mode 1 ISWs. Internal wave fields of the type described here are expected to exist in a variety of other shallow seas as well.

Citation: Bogucki, D. J., L. G. Redekopp, and J. Barth (2005), Internal solitary waves in the Coastal Mixing and Optics 1996 experiment: Multimodal structure and resuspension, *J. Geophys. Res.*, *110*, C02024, doi:10.1029/2003JC002253.

1. Introduction

[2] Internal solitary waves (ISWs) are common features of the coastal ocean [*Ostrovsky and Stepanyants*, 1989]. They can carry [*Gerkema and Zimmerman*, 1995] a significant portion of the energy resident in the internal tide (internal tides can account for up to 30% total tidal energy [*Egbert and Ray*, 2000]) and dissipate it far from their generation site. ISWs are frequently observed, as they are rather long-lived features capable of travelling tens of km before they dissipate. Owing to the difficulties inherent in sampling ISWs throughout their lifetime, their origin and their influence on shelf dynamics are poorly understood. Unfortunately, present remote observation methods are limited due to poor spatiotemporal coverage arising from cloud cover in the case of optical detection while synthetic aperture radar (SAR) is very sensitive to local wind conditions.

[3] Another hindrance to observation and characterization of ISWs is the fact that their dynamics are intricately related to the local environmental conditions on the shelf within a small radius (few kilometers) from the wave. Small changes in the mean background velocity, (e.g., 5 cm s^{-1} across a 70 m water column) or the presence of a thin stratified surface layer on the order of a few meters, can radically change the properties of low-mode ISWs, especially the nature of the wave-induced boundary layer under a wave propagating against a weak current [*Wang and Redekopp*, 2001; *Wang et al.*, 2001; *Redekopp*, 2002]. The detailed information on properties of the water column, which are necessary to accurately characterize local dynamics associated with ISWs, are usually unavailable.

[4] Fortunately, the ONR-supported multi-institutional 2-year-long Coastal Mixing and Optics experiment (CMO) provided comprehensive data on environmental conditions and ISW interactions. This experiment included remote observation by RADARSAT and ERS-2; synoptic surveys from the multisensor Sea-Soar, a towed undulating measurement platform; and Eulerian observations acquired from several moorings and bottom tripods. These concurrent observations enabled a rarely possible study of ISW propagation and interaction as well as a better understanding of events as well as the interaction between ISWs and the boundary layer. The results reported here correspond to data acquired during 1996, the first year of the CMO experiment. Several resuspension events induced by ISWs occurred

0148-0227/05/2003JC002253$09.00

during calm periods as well as during very energetic portions of the time series when the experiment site was influenced by passage of intense storms.

[5] An important result of our analysis is that, in contradiction to earlier observations [*Ostrovsky and Stepanyants*, 1989], mode 2 waves were observed frequently and they were often large enough to contribute significantly to resuspension events. Mode 2 waves seemed to be generated locally. They closely followed packets of mode 1 ISWs and were present in the record irrespective of the energetics of the water column. They did not appear to present any signature in the available SAR imagery. To the best of our knowledge, mode 2 wave packets have never been documented in SAR images of shelf regions.

[6] This study presents an overview of some interesting phenomena associated with in situ observations of long internal waves in the CMO 96 experiment, namely the observed multimodal wave dynamics and the role of these ISWs in resuspension. We begin with a description of the experiment and the mean environmental conditions. Next, we discuss possible ISW generation sites and observed directions of propagation. We propose some possible interactions between mode 1 waves and mode 2 waves and present an overview of the proposed mechanism for ISW-induced resuspension. Finally, we describe several events where both mode 1 and mode 2 waves led to pronounced resuspension, including a case of polarity switching in which an ISW packet switched from a wave of depression to a wave of elevation. We also present observations of the surface wave stress reversing the near-bottom flow and promoting resuspension.

2. Overview of Coastal Mixing and Optics 1996 (CMO 96) Experiment

[7] The site of the experiment was the ''Mud Patch'' of the Middle Atlantic Bight, the southwestern portion of George's Bank in the vicinity of 40:29.5°N, 70:30.46°W (see Figure 1). This site is approximately 110 km south of Martha's Vineyard, Cape Cod, Massachusetts, U.S.A. The water depth is approximately 70 m. Many details of the experimental design can be found in the work of *Lentz et al.* [2003].

[8] The data used in this study were acquired from the central mooring (operated by Oregon State University, OSU) [*Boyd et al.*, 1997], from Sea-Soar surveys [*Barth et al.*, 1998], and from SAR images posted on the CMO web site by *Porter et al.* [2001] (http://fermi.jhuapl.edu/cmo/cmo_index.html). The mooring contained a thermistor chain with thermistors spaced at 4 m intervals between 11 and 66 m which provided temperature measurements at 16 depths every 2 min. An ADCP measured currents between 3 m and 55 m depth [*Boyd et al.*, 1997] every 2 min. Concurrent Sea-Soar surveys provided spatial distribution of the Brunt-Väisälä frequency $N(z)$ away from the mooring.

[9] The Super-BASS (maintained by the Woods Hole Oceanographic Institution (WHOI)) [*Shaw et al.*, 2001] made frequent (few per second) acoustic measurements of the local horizontal and vertical velocity between 0.38 meters above bottom (mab) and 7 mab [*Hill et al.*, 2001].

[10] An optical tripod mooring (maintained by University of California Santa Barbara, UCSB) [*Dickey et al.*, 1998] provided (relative) measurement of the particulate loading, termed beam-C signature, at 2 mab every 7.5 min. Beam-C measures the attenuation of light (at the wavelength of 660 nm) over a 0.25 m path length. In the paper we usually plot the relative beam-C values, offset by a constant. This sometimes leads to negative beam-C values but helps to illustrate the point. At the instrument depth (68 m), the beam-C signal is linearly dependent on the particle concentration [*Bogucki et al.*, 1997]. Data obtained from the two bottom tripods (Super-BASS and optical) deployed approximately 400 m from the central mooring were very valuable to observe bottom resuspension.

[11] We focus here on a subset of CMO 96 data extending from Julian Day (JD) 235 to JD 270, corresponding to 22 August–26 September 1996. The nominal stratification during this period consisted of a prominent thermocline and the water column could be reasonably approximated as a two-layer system. Two hurricanes passed by the outer reaches of the shelf during the study period. This led to dramatic variations in environmental conditions, both in the density structure and the velocity shear.

3. Background Conditions

[12] The physical conditions at the experiment site can be divided into two major periods which differ in their mean stratification and current speed and direction. These periods are termed the ''nominal'' and the ''energetic'' period.

[13] The nominal period extends from JD 235 to JD 246 and represents climatological or quiet summer conditions on the shelf. The stratification was two-layer like with a maximum Brunt-Väisälä frequency, N_{max}, located between 10 and 20 m below the surface. The mean peak-to-peak current at 7 mab was comparable to the long time averaged tidal velocity $u_{tide} = O(5\ cm\ s^{-1})$ (Figure 2). The large ISW wave trains that reached the mooring were phase locked to the barotropic tide. There was very little cloud cover over the mooring area at this time, resulting in a strong near-surface stratified layer.

[14] The energetic period encompasses JD 246 to the end of the deployment at JD 270, a period during which the site was strongly affected by severe storms Eduard and Hortense. At the beginning of this period (JD 246) the depth of the maximum in stratification, N_{max}, descended rapidly due to increased mixing and dissipation at the surface by strong winds. The depth of N_{max} descended rapidly to a few meters from the bottom on JD 247. Solar insolation during this period was more variable due to cloud coverage, resulting in the sporadic appearance of a near-surface stratified layer. Variations in the stratification in which the maximum shifted from near-surface to depth were a consequence of forcing by both wind and solar insolation. Shifts of this nature occurred repeatedly during this period.

[15] The storm at JD 246.5 (hurricane Eduard) brought marked changes in the mean conditions (Figure 2). The peak-to-peak value of the tidal-like (low-passed) flow speed at 7 mab increased to approximately $u_{tide} = O(25\ cm\ s^{-1})$. We believe that both the increase in the current speed and the change of its pattern were due to the arrival of forced

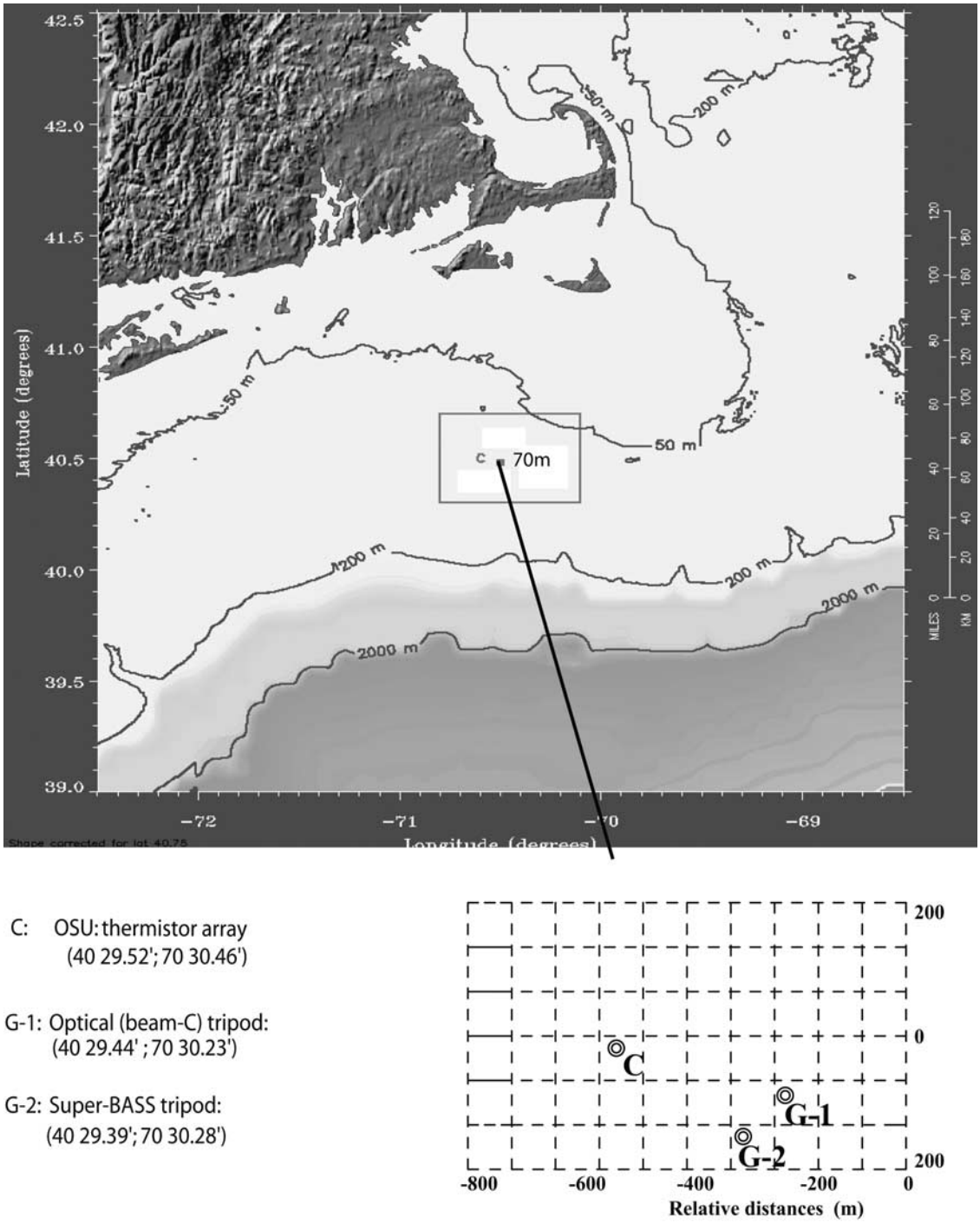

Figure 1. Coastal Mixing and Optics (CMO) mooring location with an expanded closeup of the central mooring. The data for this paper were collected from central mooring (mooring C) and from bottom tripods (G-1 and G-2).

long internal waves of mode 1. Internal lee waves were generated by the footprint of low pressure and high wind stress associated with the hurricane. The linear radiated wave field generated by this general mechanism is described by *Gill* [1982]. Hurricane Eduard traveled nearly parallel to the coast and its shoreward edge passed about 110 km from the CMO site. Its speed with respect to the bottom was approximately 3 m s^{-1}. The first baroclinic mode speed (i.e., the mode 1 long internal wave) is at most O(1 m s^{-1}). Thus the fast-moving hurricane left a radiated pattern of long internal waves in its wake. The observed frequency of lee waves relative to a stationary observer is given by $\omega^2 = f^2\ U^2/(U^2 - c_1^2)$, where U is the hurricane translational speed, c_1 is long

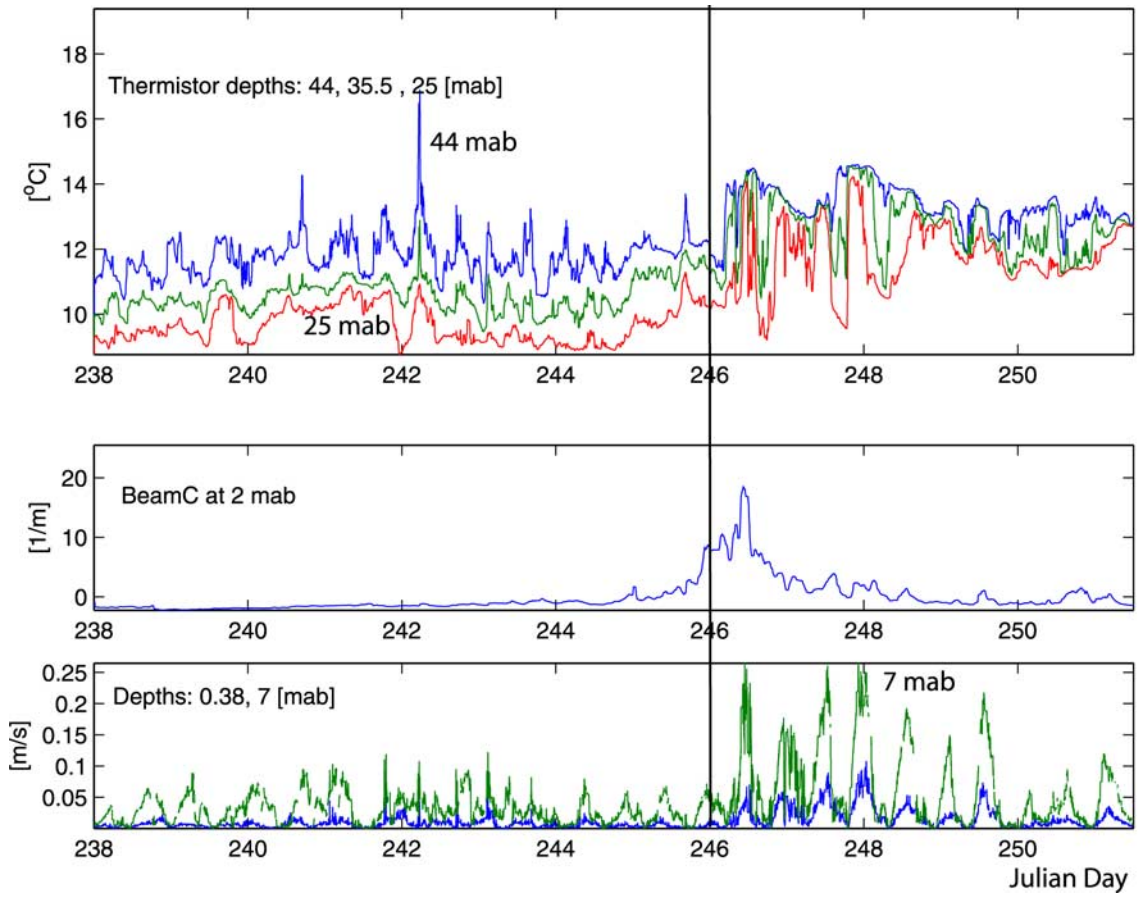

Figure 2. Time series spanning JD 238 to JD 252. (top) Temperature time series thermistors readings 26–51 m. (middle) Beam-C at 2 meters above bottom (mab). (bottom) Time series of horizontal current speed at discrete levels: 0.38 and 7 mab.

wave mode 1 speed, and here $U > c_1$ with ω close to the inertial frequency f. This, we believe, accounts for the current strength increase as in shown in Figure 2. At JD 246.5 the near-inertial oscillation propagating across the mooring location increased the near-bottom current speed up to 0.25 m s^{-1}.

[16] The ISWs passing by the mooring during this time were no longer in phase with the tide. We show later that the beam-C attained maximum values during this period, when the ISW packets interacted with the current associated with the radiated lee waves. The peak near-bottom fluctuating current appeared to be enhanced during this period (see Figure 2).

[17] The most energetic period ended after hurricane Hortense on JD 256. This hurricane was 350 km from the CMO site at its closest approach. The wind speeds at its center were weaker than those associated with hurricane Eduard (10 m s^{-1} for Hortense versus 20 m s^{-1} for Eduard) and generated longer surface waves due to greater fetch. On JD 259, after hurricane Hortense, the stratification profile consisted of the usual near-surface maximum plus an additional near-bottom maximum due to the influx of cold bottom water.

[18] Additionally, there are indications that some internal mesoscale features may have propagated through the mooring site during the experiment. For example, the Sea-Soar data taken 10–20 km away from the mooring site, occasionally recorded a deeper N_{max} (by 5–10 m) than that seen at the mooring.

4. Internal Solitary Wave (ISW) Generation

[19] The generation of ISWs is associated with time-dependent flow over topography. Here we use SAR images, a commonly applied and effective tool to locate ISW generation sites. SAR imaging of ISWs relies on the modification of the surface gravity wave field by the coherent surface strain rate induced by ISWs travelling along the wave guide of the thermocline. The organized pattern of short gravity waves can, in turn, be detected by the radar backscatter system via Bragg scattering. An overview of SAR observations of ISWs in the CMO experiment is given by *Porter et al.* [2001].

4.1. Along-Shelf Propagation

[20] The image for JD 237.1 (Figure 3) (ERS-2 Orbit 7029A, 24 August 1996, 0257 UT; beam mode: standard) during the nominal period, illustrates the propagation of two distinct ISW wave trains which were likely generated by the semidiurnal tide. Both ISW wave trains seemed to originate from the same point source and propagated eastward approximately along the shelf. The first wave train arrived at the mooring location at JD 237.1 and the second wave train had just passed at JD 237.54.

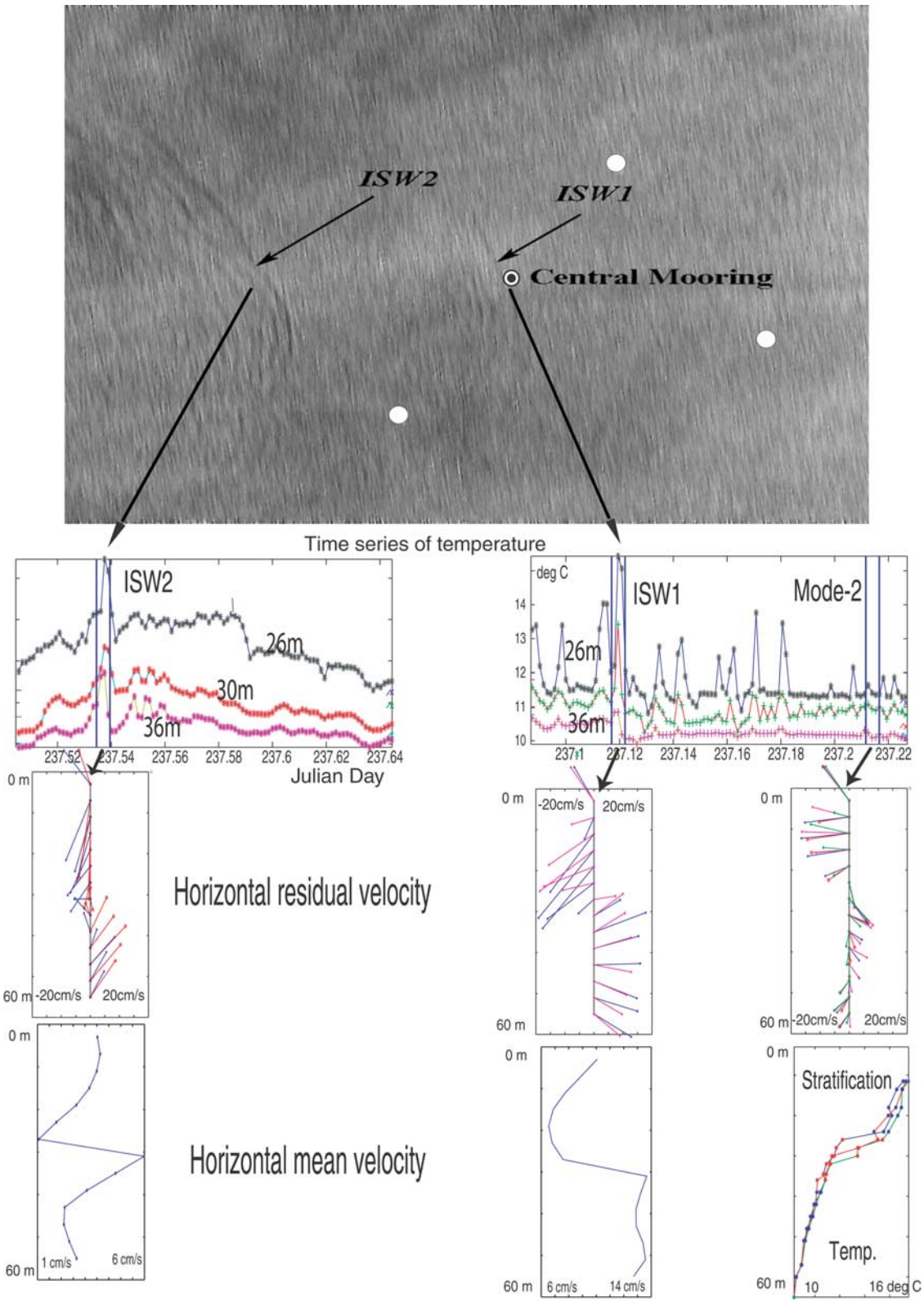

Figure 3. (top) Synthetic aperture radar (SAR) image acquired at JD 237.1. The white dots point to the location of the CMO mooring. The middle symbol pinpoints the location of the central mooring, from which the data were acquired. (middle) Observed time series of the temperature from thermistor chain from the central mooring; two distinct wave trains occurred 12 hours apart. (bottom) Vertical current structure: mean and fluctuating current at selected times corresponding to observed mode 1 wave and to the mode 2 and mode 1 waves. The stratification is shown on the right side.

[21] The leading wave of both wave trains was consistent with a mode 1 ISW (as seen in the current record observed by the ADCP). The leading wave in the first packet (passing the mooring at JD 237.1) was significantly stronger, based on the ISW-induced current registered by the mooring. This is not reflected in the SAR images; in fact the second ISW wave train seems to be stronger in the SAR image (Figure 3), possibly due to the dissipation.

[22] At the time of the SAR observation, the N_{max} was pronounced at 25 m depth at the mooring location. During the passage of the first wave train (JD 237.1 (Figure 3)) the tide in the vicinity of the ISWs was approximately barotropic (outgoing or ebb) with a speed of 17 cm s^{-1} (S. Pierce, personal communication, 1996–1999). The wave packet was approximately perpendicular to the tidal flow. The first wave train arriving at the mooring at JD 237.1 had a modal structure dominated by mode 1. Two hours later (at JD 237.23) the mode content changed and mode 2 waves appeared in the mooring data (Figure 3). The mode 2 wave was not visible in the SAR image. The succession of mode 1 leading wave(s) in the wave train followed by mode 2 ISWs seems to be characteristic of the observations at the CMO site examined to date.

4.2. Cross-Shelf Propagation

[23] In general, the ISWs observed during the CMO 96 experiment appeared to originate from many sources: see Figure 4, where they are indicated as ISW1 to ISW5. The RADARSAT image for JD 272.12 (Figure 4, energetic period) provides an example of cross-shelf propagating ISWs. Several ISW wave packets traveled north from the underwater canyon toward the CMO mooring.

[24] To pinpoint the source of these wave trains we have compared the SAR image with the calculated barotropic tide distribution prior to that time (Figure 4) (S. Pierce, personal communication, 1996–1999). We estimate that the "youngest" wave train (ISW1) was caught on the SAR image 6 hours after its inception. Hence the two most prominent ISW wave trains (ISW1 and ISW2) were likely generated during the outgoing phase (ebb) tide. In general the tide is fastest on the northeastern side of the imaged area. This coincides with observations of ISWs on the SAR image. ISW wave trains at different stages of evolution occur in the eastern part of the image, seemingly originating from nearby canyons and other topographic features. With some surprise the SAR image does not reveal any ISW wave trains in the vicinity of an another prominent canyon (east from the one marked by the arrow) and located at 280 m. The barotropic tide might have been too weak to excite internal waves or the surface conditions may have made it impossible for the SAR imagery to register ISWs.

[25] Figure 4 shows the calculated barotropic tide concurrent with the SAR image. Tidal direction was toward the shore and the speed was comparable to the strength of the ebb barotropic tidal flow (Figure 4).

[26] At the time of the SAR image, the "older" ISW wave train (ISW2) and "younger" (ISW1) were being advected north by a tidal current which is approaching 20 cm s^{-1}. Just after its generation, the "younger" wave train (ISW1) was traveling against the tidal current of 12 cm s^{-1}. The ISWs speeds can be approximated by the mode 1 and mode 2 long wave speeds for the stratification and the background shear (from the Sea-Soar, assuming homogeneous conditions). The calculated linear long wave propagation speed was 45 cm s^{-1} for mode 1 and 20 cm s^{-1} for mode 2 speed. Since ISWs are nonlinear features and their speed is amplitude-dependent, we expect the ISW wave packets to be propagating faster than the corresponding long wave speeds. Mode 1 solitary waves were faster than the tide, but the mode 2 solitary waves were roughly of the same speed or slightly slower.

[27] The SAR image of the vicinity of the central mooring (Figure 4) shows ISW-like features propagating diagonally across the image. In general the CMO site recorded ISWs travelling from different directions (for example, ISW5), thus suggesting that although ISW generation may be predominantly tidally driven (before the storm period) they are also likely to be topographically generated by current interaction with different topographical features [*Bogucki et al.*, 1997].

5. Sources of Mode 2 Waves

[28] It is not clear whether the mode 2 waves observed in our data were generated in the same place as mode 1 waves or if they were generated as a result of environmental inhomogeneities or nonlinear modal interactions. In the case of the former, mode 2 waves would appear at a well-defined origin, while in the latter case they would be created continuously during the mode 1 wave lifetime. Here we propose that the frequently observed second mode ISWs are due to a local mechanism for intermodal energy transfer. This is in contrast to the mechanism of mode 2 generation at the shelf break proposed by other researchers [e.g., *Lamb*, 1994].

[29] The motion of an ISW relative to the bottom can be expressed as a sum of the wave speed and the spatially varying barotropic tide. Hence the distance s covered by the ISW away from the source can be expressed as

$$s = c_0 t + \int_0^t u_{\text{current}}(x, t')dt', \tag{1}$$

where c_0 is the mode 1 or mode 2 wave speed, $u_{\text{current}}(x, t)$ is the tidally dominated current, and x is a Lagrangian coordinate. The distance s from the shelf break to the mooring is approximately 63.5 km. The barotropic tidal current is shown on Figure 4 for the time of the image acquired by SAR and 6 hours prior to SAR image acquisition. The wavelength of the barotropic tide (order of a few thousand kilometers) and its speed (approximately a few hundred kilometers per hour) is much larger than the corresponding ISW length and speed. The current associated with the tide is at most of order of a few tens of centimeters per second.

[30] The above equation for the case of ISW riding on a tidal current can be simplified to its Eulerian representation if we notice that

$$s = c_0 t + \int_0^t \{u_{\text{current}}[x(t'_0), t'] + \nabla u_{\text{current}}[x(t'_0), t'](dx/dt') \cdot (t' - t'_0) + O(t' - t'_0)^2\}dt', \tag{2}$$

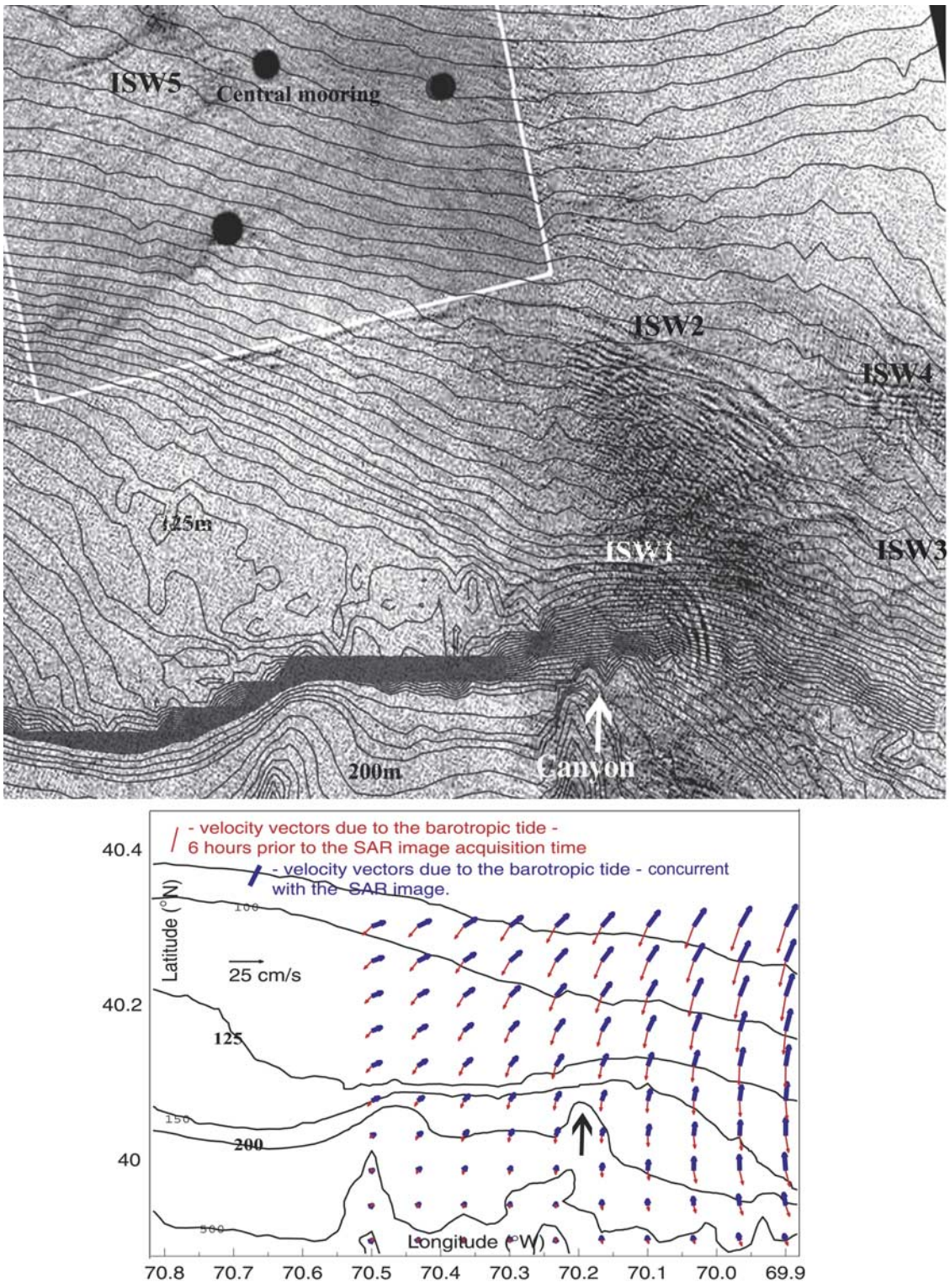

Figure 4. (top) SAR image taken at JD 272.5 with overlayed bottom topography and location of the CMO mooring. The central mooring location is represented by the topmost black dot. (bottom) Calculated tide (approximately the same area as the SAR image) for JD 272.5 (vectors pointing north) and calculated tide during internal solitary wave (ISW) generation 6 hours earlier (vectors pointing south). Tidal calculations were provided by S. Pierce. The underwater canyon at 200 m depth (marked with an arrow) seems to be the source of the two visible ISW wave trains.

where ∇ operates on the Lagrangian coordinates and t'_0 is an initial observation time.

[31] Carrying out the leading term estimate of equation (2), the u_{current} is at least an order of magnitude larger than the term associated with the spatial derivative showing that to the first-order Eulerian and Lagrangian approach are equivalent. We then can write the distance s covered by the ISW as: $s = c_0 t + \int_0^t u_{\text{current}}[x(t'_0), t']\, dt'$.

[32] The $u_{\text{current}}[x(t'_0), t']$ is an Eulerian current expressed in local coordinates. We can express (based on our observation) the local current u_{current} as a sum of a tidal periodic component and a spatially (along the soliton footprint) varying local current $U(x)$. Hence the tidally dominated current contribution to the ISW path can be written as: $\int_0^t u_{\text{current}}(t')\, dt' = \int_0^t (u_{\text{tide}}(t') + U(x))dt'$, where $u_{\text{tide}}(t) = 0.25 * \sin(2\pi t/T)$ (m/s), and T is the tidal period (the dominant M2 tidal component is around 12.42 hour). The integrated contribution to the soliton travel path over the tidal period is less than 3.5 km (i.e., $|\int_0^t u_{\text{tide}}(t')dt'| < 3.5$ (km)). The travel time can be expressed as: $t = s/c_0 \cdot (1 - 1/s \int_0^t u_{\text{tide}}(t')dt')/(1 + (U(x)/c_0)$. The observed ratio $U(x)/c_0$, the ratio of the spatial subtidal current component of the wave speed, is around 0.3 for mode 2 and 0.1 for mode 1 in the mooring vicinity. As we move away from the source of the ISW ($s \rightarrow \infty$) the term $(1 - 1/s \cdot \int_0^t u_{\text{tide}}(t')dt')$ approaches 1.

[33] The travel time t_{travel} for the ISW to arrive at the mooring can be expressed as: $t_{\text{travel}} \approx (s/c_0) \cdot (1 + U(x)/c_0)^{-1}$, assuming a distance $s = 63.5$ km to the mooring and c_0 as the appropriate wave speed. The dependence on location in $U(x)$ is left to indicate that calculations should generally assume spatial variation of the subtidal current over the shelf. We present here only the order of magnitude estimates. According to these calculations, the mode 1 ISW requires approximately 1.7 days to arrive to the mooring and the mode 2 ISW requires 3 days from this generation site. The arrival time is sensitive to the wave speed and very sensitive to the ratio of the local subtidal current to ISW wave speed. Since the subtidal current variations [*Pierce et al.*, 1998] can be larger than the mode 2 ISW speed, especially near the shelf break, the mode 2 ISW arrival time depends strongly on the local current conditions along the wave trajectory. Furthermore, since the average time difference between the arrival to the mooring of ISWs of mode 1 and mode 2 is approximately one day, and since the waves can experience very different current conditions, local variations in the subtidal current along the wave trajectory are likely to further increase the time difference of their arrival. Thus the correlation between mode 1 and mode 2 ISWs at the mooring site should be weak. This is contrary to observations from the CMO experiment as presented below and points to mode 2 ISW being generated most likely via intermodal energy transfer.

6. Coupling Between Mode 1 and Mode 2 ISWs

[34] The CMO observations provide evidence that mode 1 and mode 2 ISWs are frequently coupled even under different background conditions. The coupling between modes can have considerable impact on near-bottom flow conditions. Mode 1 ISWs frequently lead to separated flow in the wave-induced bottom boundary. Flow separation under the ISW footprint has previously been associated with very large resuspension events [*Bogucki et al.*, 1997]. The CMO 96 experiment confirms earlier observations and additionally reveals the prominent role of mode 2 ISWs in resuspension.

[35] The appearance of a mode 2 ISW behind an advancing mode 1 wave can be explained by the interaction between a "clean" mode 1 ISW and spatial inhomogeneities in the environment forming the waveguide. Relevant inhomogeneities might include variable depth of the water column, local topographical features, or spatial variations in the stratification or the velocity shear.

[36] There are a number of plausible hypotheses to explain ISWs of mode 2 following mode 1 waves. One example is soliton-soliton resonance associated with higher-order terms arising in a multiscale expansion of the Euler equations.

[37] Soliton-soliton resonance occurs when the mode 1 and mode 2 phase speeds are close, a condition that occurs in a structured thermocline, especially when near-surface and near-bottom peaks in the Brunt-Väisälä frequency are present. Another potential mechanism for local generation of mode 2 waves involves energy transfer from mode 1 to mode 2 waves via nonlinear coupling when mode 1 waves deform in the presence of inhomogeneities in the depth or in environmental conditions [*Gottwald and Grimshaw*, 1998].

7. ISW Mechanism for Resuspension

[38] The passage of ISWs in the CMO observations are frequently associated with near-bottom increases in turbulent kinetic energy and particle concentrations in the wave footprint. It is our thesis, although not essential to the primary objective of this paper, that these local effects are a manifestation of a global instability [*Hammond and Redekopp*, 1998]. This global instability occurs within the benthic boundary layer (i.e., the wave-induced boundary layer in the footprint of the wave) triggered by the passing wave packet. Since reference is made in what follows to aspects of global instability in describing selected events in the CMO data set, a brief discussion of several underpinnings of this proposal is given to provide an interpretive framework for the occurrence of sudden increases in the beam-C signature simultaneous with the arrival of an ISW packet.

[39] Global instability is an entirely intrinsic dynamics, i.e., without any external stimulation, that occurs spontaneously in a flow. The specific unstable flow relevant to this discussion appears in the wave-induced boundary layer whenever the instability threshold is exceeded.

[40] The onset of global instability is nominally associated with the appearance of an internal region of local absolute instability of sufficient spatial extent, or at least a point of absolute instability, in a spatially developing flow [*Huerre and Monkewitz*, 1990; *Pier et al.*, 1998]. Further, the instability is termed global because it gives rise to a coherent dynamics that is synchronized over length scales encompassing the entire flow state (e.g., a separation bubble forming in the wave-induced boundary layer). This type of instability appears in boundary layers only when regions of sufficiently strong reversed flow (i.e., separation) exist [*Hammond and Redekopp*, 1998]. Flow separation appears

in the context of ISWs near the front of a wave of elevation, as seen in the simulations of *Bogucki and Redekopp* [1999] or *Stastna and Lamb* [2002]. It can also appear following the crest of a wave of depression where the wave-induced boundary layer develops in a region of adverse pressure gradient. The possibility of separation in this latter case was discussed by *Wang et al.* [2001] and conditions needed to trigger a global instability in such wave states were estimated, but no direct simulations were available at that time to reveal explicitly the presence of a global instability in the wave-induced boundary layer under a wave of depression. However ongoing simulations of the wave-induced boundary layer under solitary waves of depression show very clearly the onset of global instability when the wave amplitude exceeds a threshold value (P. Diamesses and L. G. Redekopp, Internal solitary wave induced global instability in shallow seas, submitted to Journal of Physical Oceanography, 2005).

[41] A representative case is shown in Figure 5. The particular wave state shown in Figure 5 corresponds to that occurring in a wave guide with an upper mixed layer, a prominent seasonal thermocline positioned at about one-quarter of the depth, and a smooth transition to a permanent thermocline extending all the way to the bottom of the wave guide. The striking appearance of an intermittent shedding of vortices which rise into the stratified water column is typical of the onset of global instability in the separated, wave-induced boundary layer. It is our thesis that the characteristic dynamics within the separated ''bubble,'' with its associated synchronous shedding of vortices are responsible for resuspension and vertical transport of sedimentary material stimulated by ISWs.

[42] Although the flow in the boundary layer under weak wave conditions may be unstable based on a local instability analysis, the spatially developing nature of the flow inhibits any streamwise growth of unstable disturbances and, consequently, no intrinsic dynamics is observed (i.e., the flow is globally stable). The situation changes dramatically when the amplitude of an ISW exceeds a critical value which is intricately related to the generation of a sufficiently strong back flow velocity internal to the induced separation bubble. Some results showing the connection of the threshold amplitude as a function of the Reynolds number obtained from direct numerical simulation for a specific flow model are presented by *Wang and Redekopp* [2001]. From another point of view, instability theory applied to a simple model of separated flow in a stratified environment can be used to estimate the critical back flow velocity, as a fraction of the external velocity (see Figures 5a and 5b). The critical back flow velocity is found to be approximately 11% [*Redekopp*, 2002]. In the presence of wave packets, where periodic regions of separation may appear, requirements for global dynamics are even less stringent [*Wang and Redekopp*, 2001] and global dynamics may appear with smaller back flows.

[43] The point deserving emphasis is that the resuspension criterion advanced here is a ''threshold'' mechanism, one which is triggered when wave amplitudes are sufficiently large to create the required internal state in the wave-induced boundary layer. Of course, the critical value of wave amplitude varies with environmental states (i.e., background current and shear and the ISW mode shape), but it is important to stress that the global instability mechanism for onset of significant resuspension action is not a ''proportional'' mechanism in which the effect varies continuously with wave amplitude. The strong temporal and spatial coherence of this sort of global dynamics is, we believe, the primary contributor to the episodic resuspension events that appear concomitant with ISW packets as documented in subsequent sections.

8. Resuspension by ISW Packets

8.1. Resuspension and Global Instability Under Mode 1 ISW

[44] Figure 6 presents data pertaining to an episode of resuspension stimulated by a packet of internal solitary waves consisting of mode 1 waves of depression. Figures 6a–6e provide a time history of the same event measured by different instruments. Figure 6a shows the output from four representative thermistors positioned between depths 22 and 44 mab (the water depth is 70 m). Figure 6b exhibits the relative beam-C signature measured at a level 2 mab. Figure 6c displays the wave-induced current measured at 0.38 and 7 mab. The directional phase of the bottom current shown in Figure 6c is plotted in Figure 6d.

[45] The solitary wave packet shown in Figure 6 propagated through the mooring site during the ''nominal'' period, that is, before the passage of hurricane Eduard at JD 246.5. A sequence of similar packets appeared quite cyclically during neighboring days surrounding this episode, arriving essentially in phase with the tide. The dominant wave peak occurred at the site shortly after JD 242.21. The ambient stratification during the passage of this packet was inferred from a Sea-Soar pass 20 km away and presented a pronounced maximum of $N = 0.03\ s^{-1}$ at approximately 15 m depth. The long wave phase speeds, consistent with wave-induced observed current, were 40–44 cm s^{-1} for mode 1, and 16–23 cm s^{-1} for mode 2 (Appendix A).

[46] The relative beam-C signature at 2 mab shown in Figure 6b increased with the appearance of the peak wave in the packet. The (relative) increase in beam-C of 0.4 m^{-1} is fairly significant, corresponding to a light *e*-folding absorption distance of 2.5 m. The extended time record shows that high beam-C values persisted for a couple hours and fell to around 60% of the peak by JD 242.4. The peak value of the wave-induced horizontal velocity approached 12 cm s^{-1} at 7 mab.

[47] A more detailed examination of the time series shows that the ISW propagated nearly parallel to the local current (0° being in the wave direction) and that the induced current was reversed up to 1.1 mab (Figure 6 (bottom right)), as schematically depicted in Figure 5a.

[48] The maximum value of the back flow below that depth was 0.25 cm s^{-1} (not shown here) as compared to the mean flow of 2.5 cm s^{-1}. The magnitude of the back flow was approximately 10% of the mean flow indicates that the associated ISW suggests that the local instability may be of absolute type and thus able to trigger a global instability under the wave footprint. The ISW-induced flow direction was undisturbed (unmodified by the instability) above 2.2 mab indicating that the vertical extent of the separation bubble was somewhere between 0 and 1.1

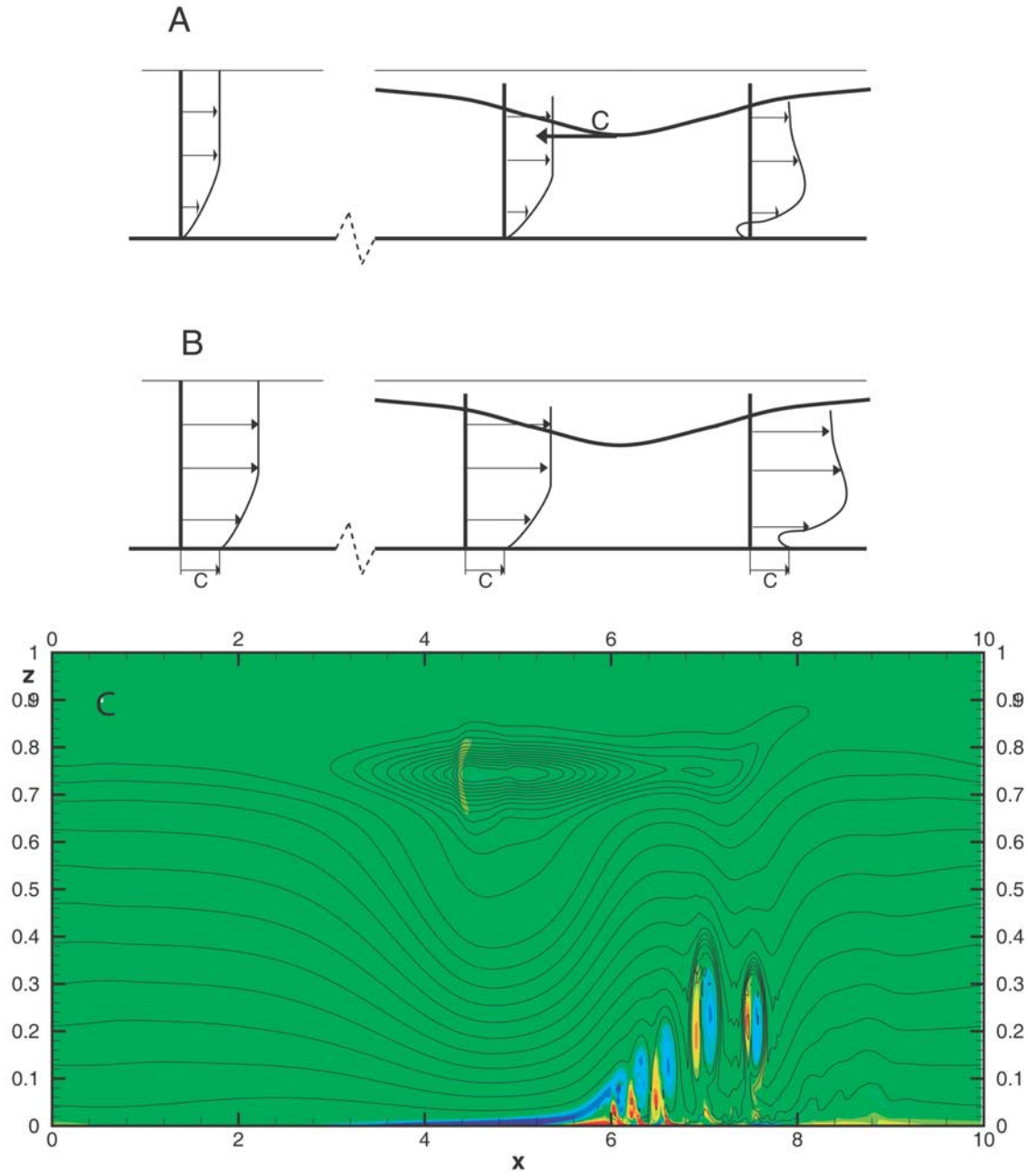

Figure 5. Schematic of the flow under the footprint of a solitary wave of depression. (a) In a bottom fixed frame. (b) In a wave fixed frame. (c) A snapshot of the globally unstable, wave-induced boundary layer under an ISW of depression propagating to the left in a stationary, continuously stratified ambient state. The flow is viewed in a frame moving with the wave, and the black lines are total density isopycnals with superimposed vortices (the blue or red areas correspond to the flow with + or − vorticity sign). The vorticity generated in the wave-induced boundary layer is seen to roll up and erupt from the separated flow in the lee of the wave, where the induced flow experiences an adverse pressure gradient.

to 2.2 mab. The near-bottom vertical velocity fluctuations (Figure 6e) associated with the reversal in flow direction were enhanced. Furthermore, the highly fluctuating bottom velocities were sustained as the trailing waves passed the tripod as were the increased beam-C values. Decreased benthic activity followed JD 242.35 as the trailing waves in the packet left the tripod. We propose that the rise in turbulent kinetic energy and beam-C under the wave packet is a manifestation of a global instability in the benthic boundary layer triggered by the passing packet.

8.2. Mode 1 Resuspension JD 243.1

[49] This resuspension event takes place during the "nominal" period at JD 243.1. Figure 7 shows the time series presented in similar convention to previous figures.

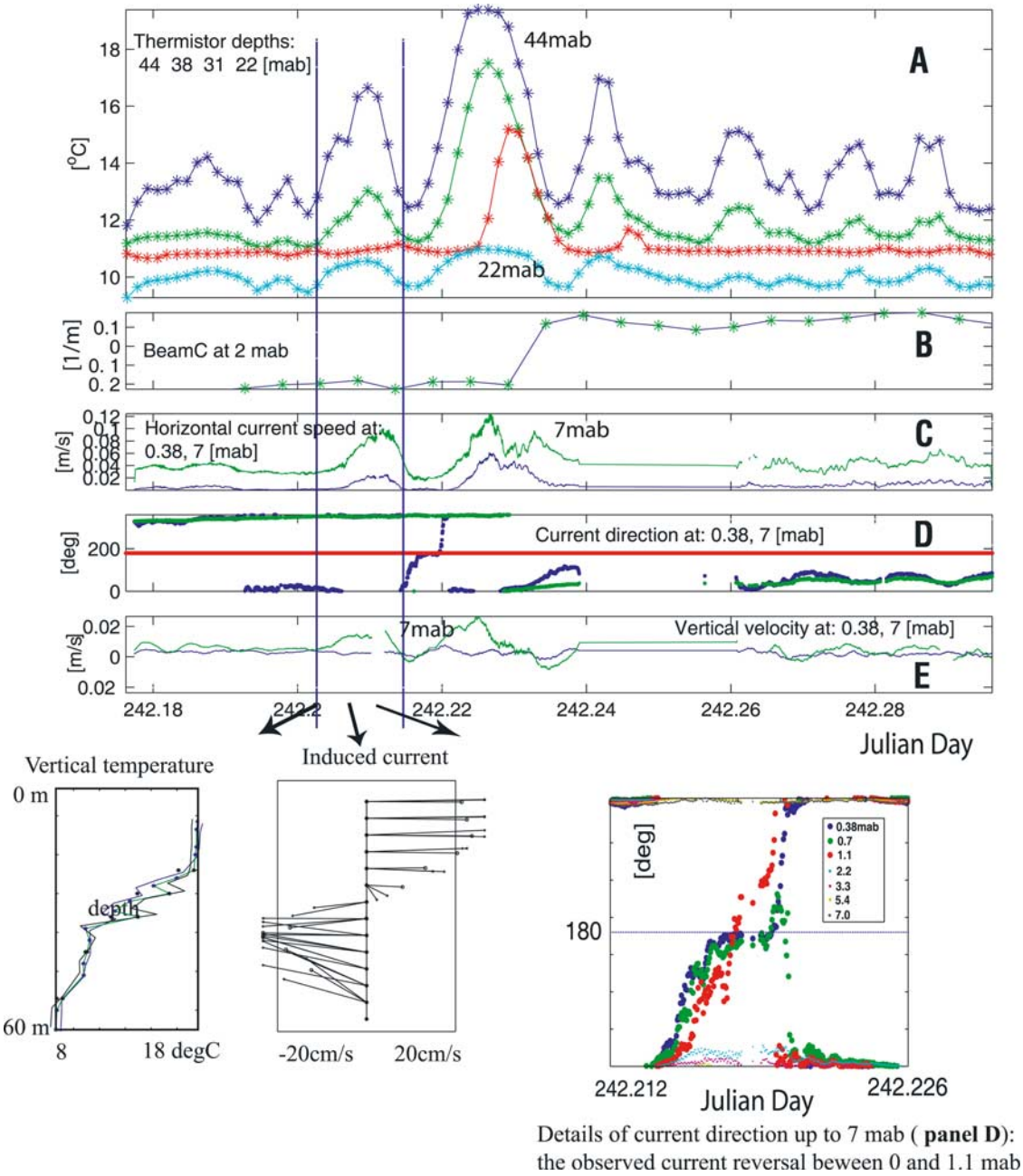

Figure 6. Resuspension event associated with mode 1 ISW. (a) Time series of the temperature from the thermistor chain. (b) Beam-C at 2 mab. (c) Current velocity 0.38 and 7 mab. (d) Current direction (0°–360°). (e) Vertical velocity 0.38 and 7 mab. (bottom left) Distribution of the vertical temperature. (bottom middle) ISW-induced current for the first ISW in the wave train. (bottom right) Details of near-bottom current reversal.

[50] The peak horizontal velocity within 0.38 and 7 mab was at most 15 cm s^{-1}. The second ISW was associated with higher near-bottom particle concentrations as seen in the relative beam-C increase by 0.6 m^{-1}, corresponding to strong resuspension. The ISWs were oblique to the local current and had an amplitude of about 15 m (maximum isopycnal displacement at 20 m below the water surface). Superimposing the wave-induced velocity on the projection of the tidal current along the ISW trajectory led, in the case of the analyzed ISW, to reversed flow near the bottom at JD 243.115. The mean current projected onto the ISW generated flow shows that the reversed current was well above the 10% threshold requirement for the onset of the global instability under the wave footprint. An additional check for the possible existence of the global instability can be obtained by examining the time series of vertical velocities at 0.38 and 7 mab depth. The magnitude of the vertical velocities are of order 0.1 cm s^{-1}, and their directions were opposite (i.e., pointing up at 0.38 mab and pointing down

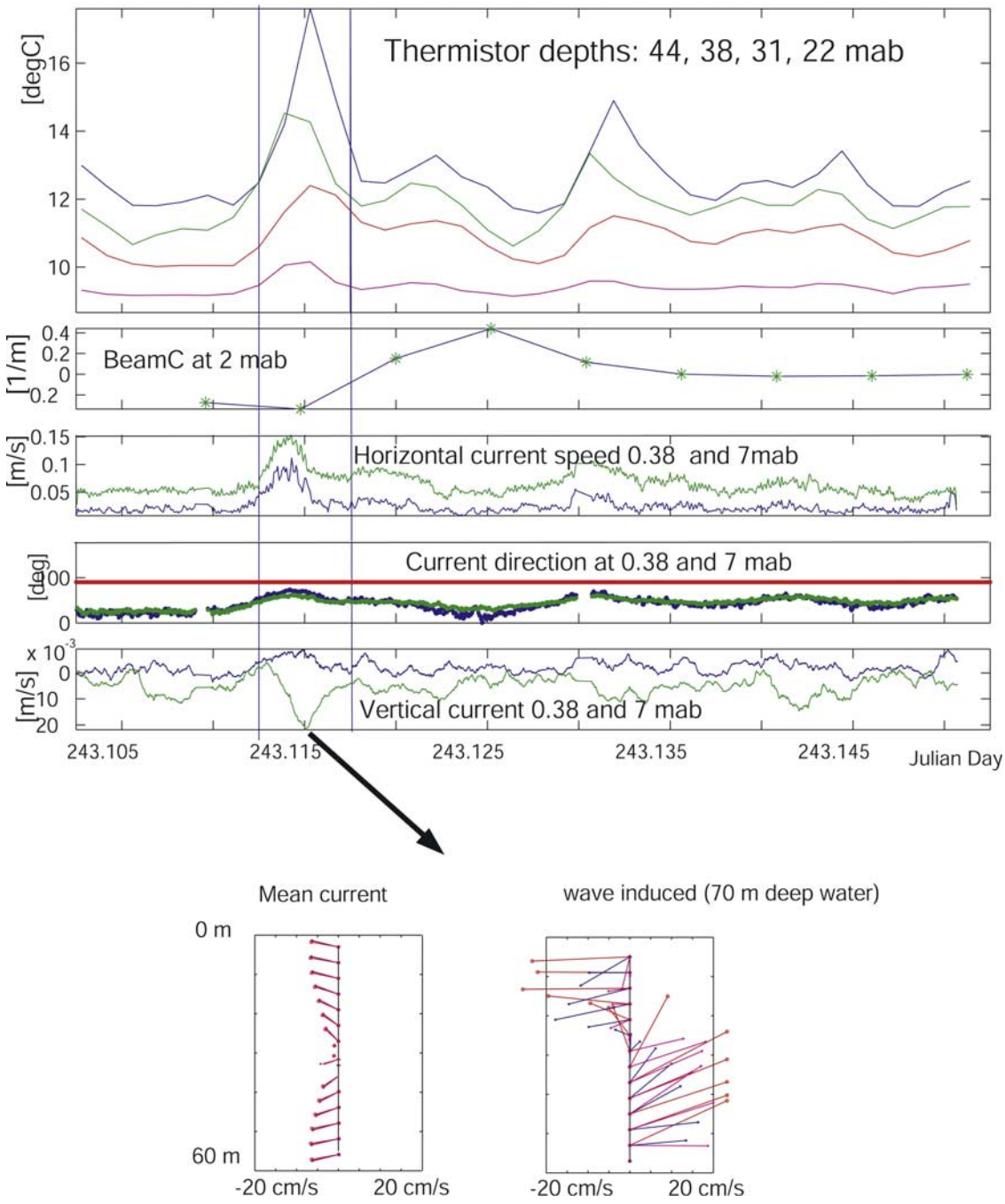

Figure 7. Resuspension event associated with a mode 1 wave. (top) As in Figure 6. (bottom left) Mean current. (bottom right) ISW-induced current.

at 7 mab, at the ISW trough). More detailed analysis indicates that the separation bubble extends up to at least 3.3 mab, but is below 5 mab.

8.3. Bottom-Trapped Mode 1 ISW

[51] One of the most spectacular resuspension events by a bottom-trapped mode 1 ISW was observed at JD 259.15 (Figure 8), one day after passage of hurricane Hortense [*Dickey et al.*, 1998].

[52] The modal structure of the ISW is unclear in the ADCP-measured $u'(z)$ data due to contamination by surface waves. The long wave properties can be inferred from the background mean shear and density profiles. The ISW was slightly oblique to the mean flow (at an estimated angle of 60°). The mean stratification presented two maxima, one near-bottom and one near-surface. The leading edge of the leading ISW was visible in the near-bottom current record before the tripod acquisition system was temporarily switched off. Judging from the thermistor chain readings (temperature time series), the leading ISW was a long wave of mode 1. As calculated for this type of stratification (see Appendix A), the mode 1 or mode 2 wave, due to high curvature of eigenfunction, is likely to generate a strong near-bottom current.

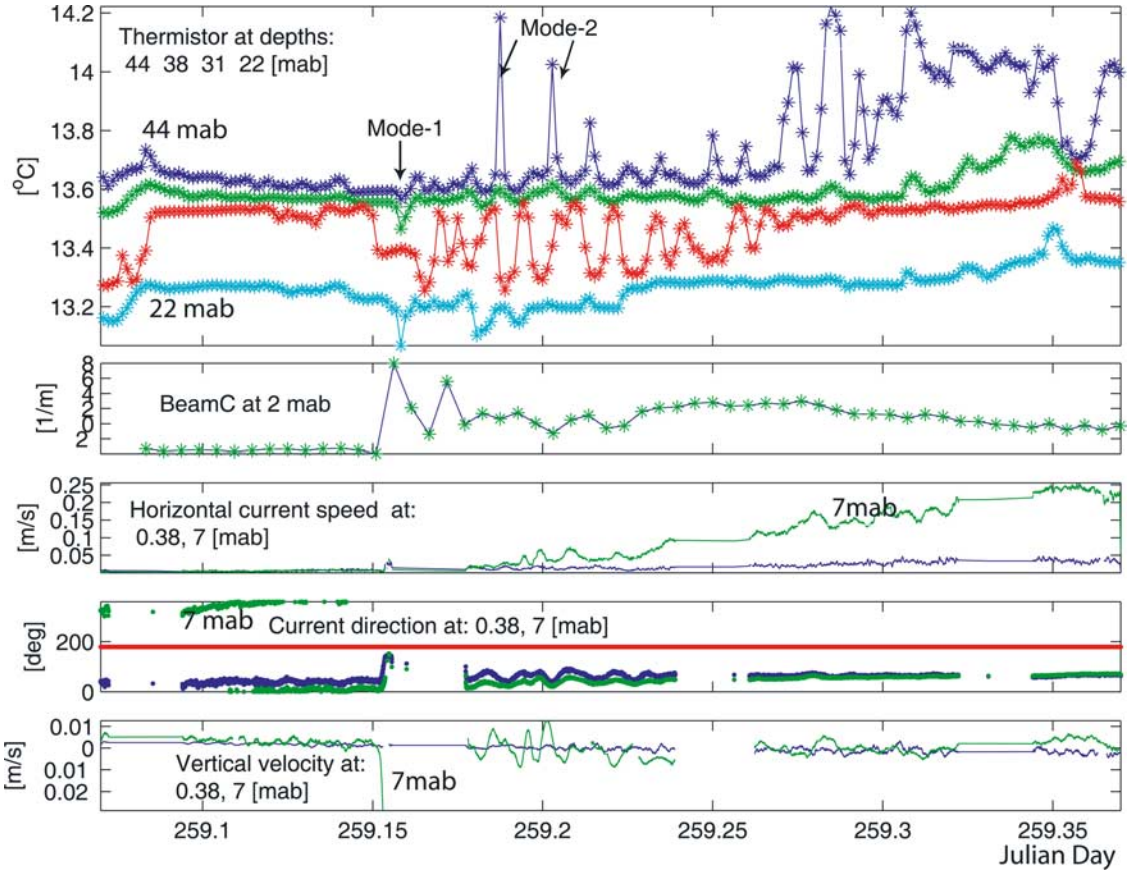

Figure 8. As in Figure 6. The mode 1 wave is followed by a mode 2 wave.

[53] The leading edge of the ISW observed at JD 259.15 was large enough to temporarily reverse the current (by 180°) before the tripod instruments were shut down. The ISW-induced current velocity was at least 4 cm s^{-1}. The vertical velocities were at least 1 cm s^{-1}. The related thermocline displacement was 5 m at 60 m depth, corresponding to a mode 1 ISW of at least 5 m amplitude. By reversing the near-bottom current, sediment was resuspended and beam-C increased almost instantaneously to the value of 10 m^{-1}. Thereafter, the sediment concentration decreased steadily.

[54] A more detailed analysis of horizontal and vertical velocity time series shows that the separation bubble extended up to 1.1 mab. In addition the horizontal velocity time series showed an organized vortex-like structure within the separation bubble. Its presence is consistent with numerical simulations of a global instability under the footprint of the soliton. Owing to proximity of the extrema of the eigenfunction for either mode to the bottom boundary, the ISW-induced velocities are enhanced. The vertical extent of the separation bubble is smaller here than in the previous example (1.1 mab). Numerical simulations of the flow in separation bubbles show that larger near-bottom shear can result in more compact and energetic global instabilities.

[55] The modal structure changed soon after passage of the mode 1 wave. At JD 259.18 (1/2 hour later) mode 2 ISWs appeared in data from the thermistor chain and the ADCP-measured $u'(z)$ (Figure 8). The water column stratification during this example has a very interesting property: the eigenmode speeds of mode 1 and mode 2 were nearly the same, which suggests the possibility of a resonant interaction between mode 1 and mode 2. The observation of wave interaction was obscured by the change in surface wave-induced mean shear from the current speed 20 cm s^{-1} 60 mab (10 m below the surface) to 5 cm s^{-1} 15 mab.

8.4. Resuspension by a Mode 2 ISW at JD 243.37

[56] Data shown in Figure 9 illustrates the effect of a mode 2 ISW on the bottom as well as additional features of ISW wave trains. The mode 1 wave train dominated the internal wave field until approximately JD 243.2 when a mode 2 structure became evident. The disturbance passing over the mooring changed from a mode 1 structure to a mode 2 structure gradually over a time interval of an hour. By JD 243.25 mode 2 waves dominated the vertical structure of the disturbance field. The vertical distribution (between the surface and 60 m depth) of the horizontal component of the wave-induced current corresponded to a mode 2 structure. The induced current was of order 8 cm s^{-1}; the vertical speed w' was order 1 cm s^{-1}; and the characteristic timescale was 0.5 N^{-1}. Mode 2 waves in the time record were generally twice as wide as mode 1 ISWs due to the different wavelengths and smaller wave speeds.

[57] At JD 243.37 the mode 2 wave (see Figure 9) was large enough (maximum isopycnal displacement at 40 m corresponds to 10 m wave amplitude) to reverse the

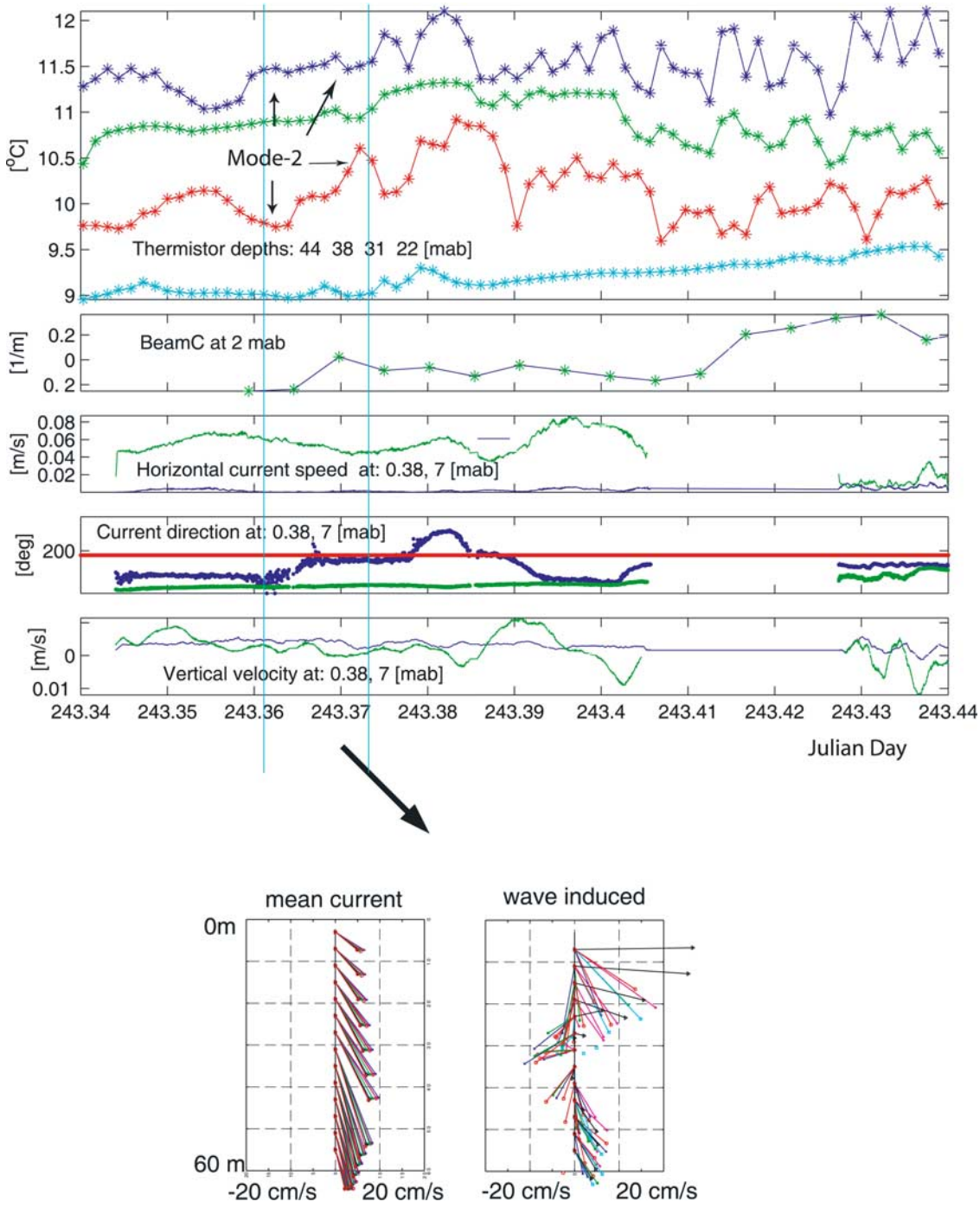

Figure 9. (top) As in Figure 6. (bottom left) Mean. (bottom right) ISW-disturbed currents.

near-bottom current. The near-bottom horizontal current up to 1.1 mab opposed the mean current. The observed vertical structure of the disturbances was similar to the vortex structure observed in the numerical simulations of global instabilities under a long wave footprint and exhibited in Figure 5.

[58] High concentrations of particles near the bottom were associated with this observed vortex structure. The passage of this structure and the associated increase in beam-C signature suggests that the postulated resuspension mechanism is quite efficient, even at relatively small induced current speeds of around 2 cm s^{-1}. It should be noted that there appear to be slight timing leads/lags between measurements made on different platforms. Consequently, a precise correlation between the flow velocities and direction reversals and the wave crest or trough is not possible at this time.

8.5. Resuspension by a Mode 2 ISW at JD 266.8

[59] A resuspension episode associated with a mode 2 ISW at JD 266.8 is shown in Figure 10. The ISW wave train arrived at the mooring site approximately ten days

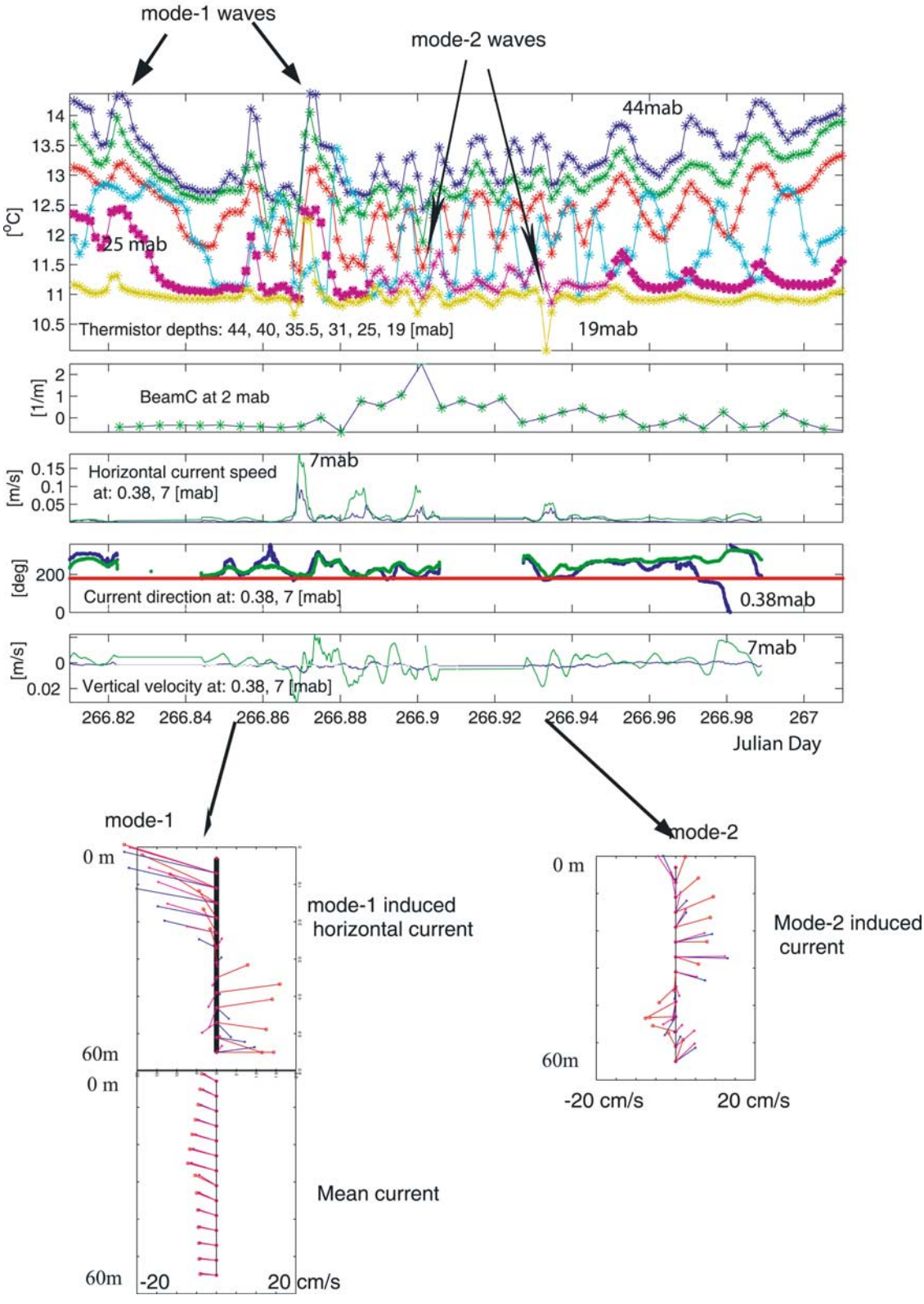

Figure 10. Mode 2 wave-related resuspension. (top) As in Figure 6. (bottom) ISW-induced current.

following the passage of hurricane Hortense, that is during the energetic period. The hurricane significantly modified the structure of the thermocline, creating a double maxima in the Brunt-Väisälä profile.

[60] The local maximum in stratification at about 10 m depth resulted from restratification following the intense storm. The near-bottom stratification had a local peak at an elevation of about 20 mab. The stratification in the mid-

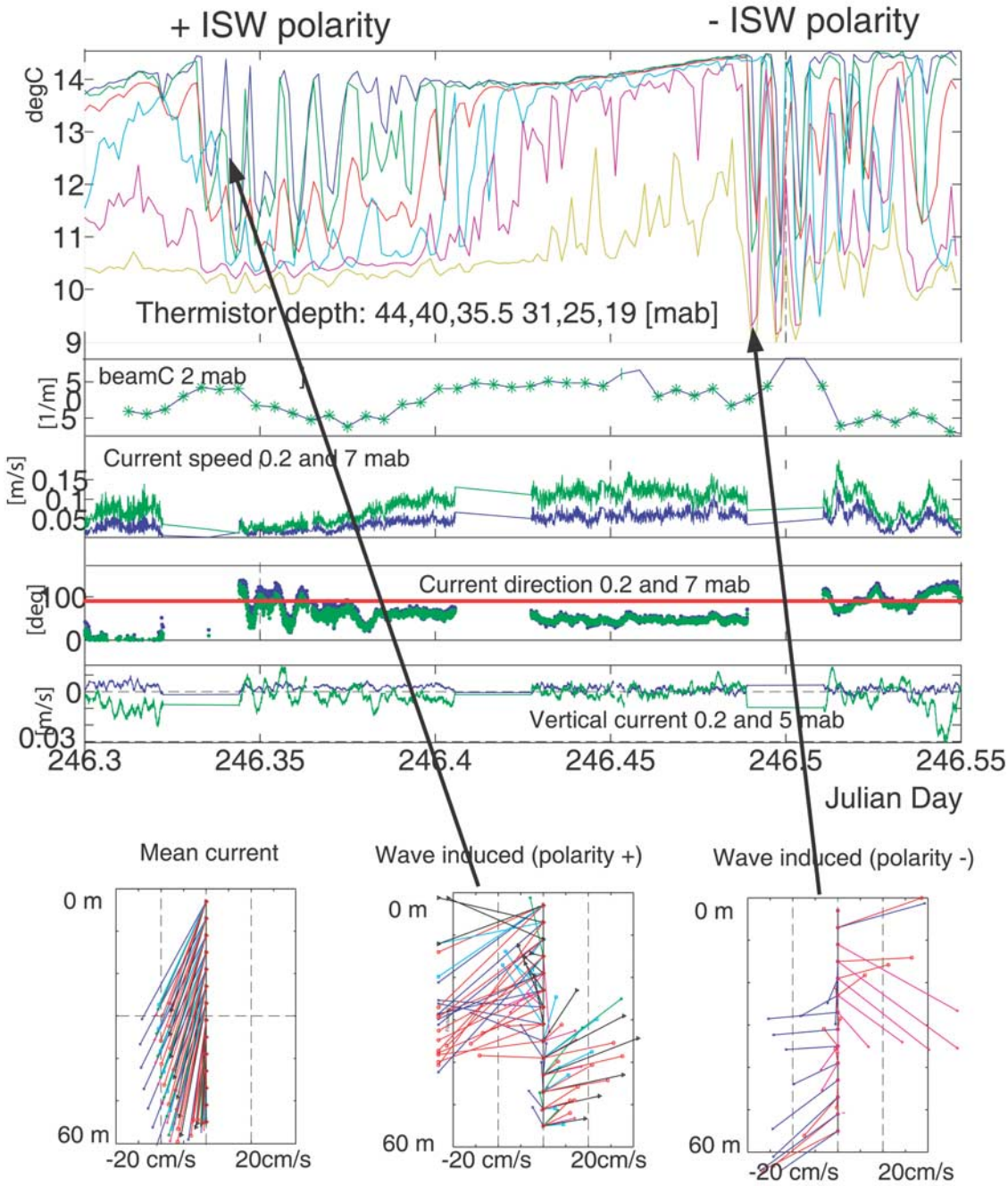

Figure 11. ISW of opposite polarity. (top) As in Figure 6. (bottom left) Mean current. (bottom right) ISW-induced current.

depth region was clearly weaker than either that near the top or that near the bottom. The mean current at the arrival time of the packet consisted principally of a barotropic tidal current of approximately 12 cm s^{-1} over the upper 30 m with a slight vertical shear over the bottom half of the water column. The packet propagated in the direction opposite to the tidal current. Under these conditions the wave-induced velocity promotes flow reversal in the boundary layer.

[61] Figure 10 contains five panels with a time series analogous to previous figures. The strength of the beam-C signal increased with the appearance of the mode 2 ISW in the packet. It is clear that the wave-induced velocity of 15 cm s^{-1} was sufficient to reverse the direction of the bottom current. The fluctuating vertical velocity near the bottom and the beam-C increased during the reversal in flow direction. The extended data record indicates decreased benthic activity after the trailing waves in the packet left the tripod at around JD 266.92.

[62] The front of the packet arriving at the site at JD 266.8 consisted essentially of mode 1 ISWs of depression. The eigenfunction for these waves was fairly broad and isotherm displacements extended over most of the water column. The beam-C signal and the induced bottom velocity under these waves was negligible. The waves are large enough to

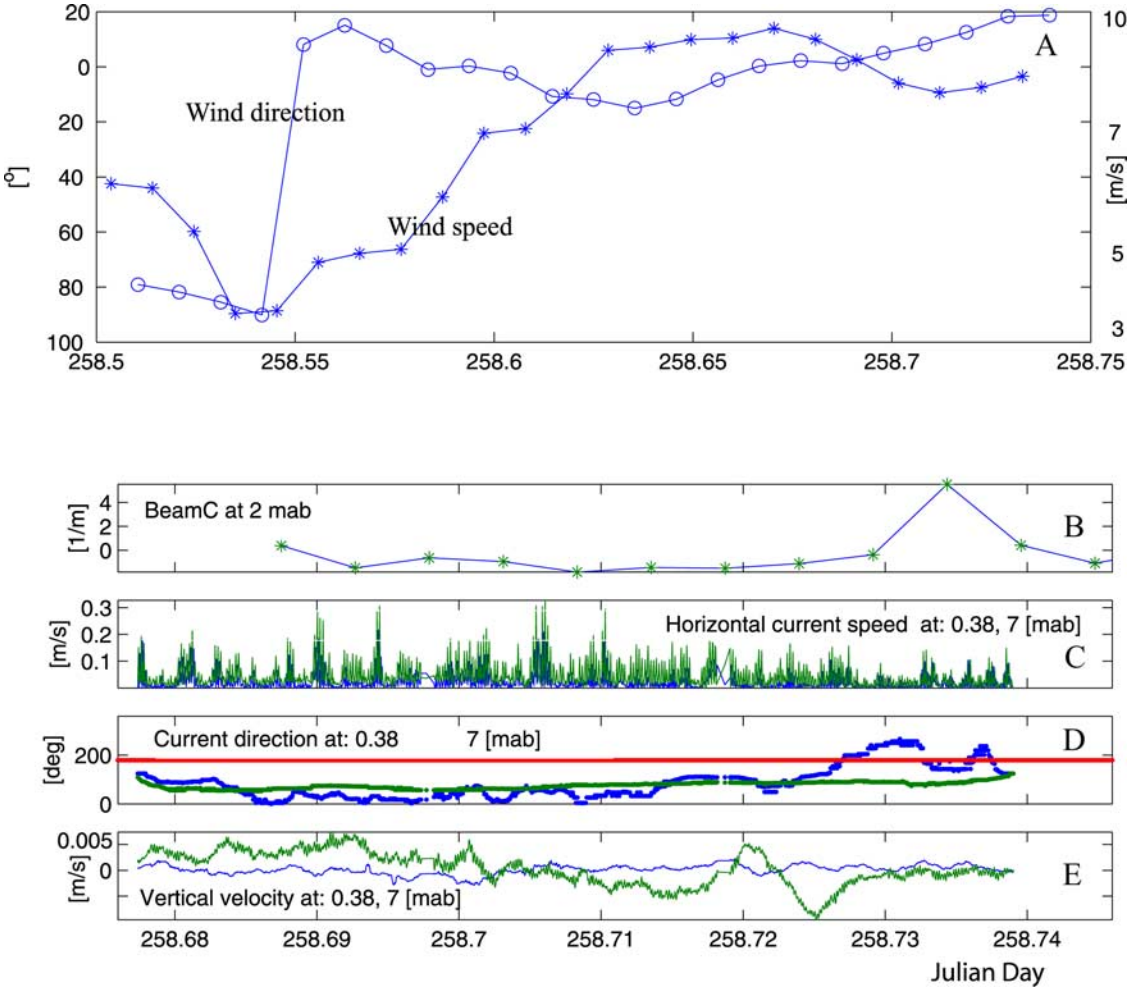

Figure 12. Change of wind stress–related resuspension. (a) Wind direction and speed. (b–e) As in Figure 6.

possibly lower the stability of the water column to induce mixing (temperature time series from 25 mab crosses several other temperature plots, e.g., Figure 10 (top panel)).

[63] However, at about JD 266.9 the modal content of the packet suddenly changed, along with the polarity of the isotherm displacements at lower levels. The disturbance velocity profiles show that mode 2 ISWs clearly emerged simultaneously with a pronounced increase in induced bottom velocity (the third panel indicates velocities up to 15 cm s^{-1}). Fluctuating velocity data from the bottom-fixed ADCP reveals mode 2-induced currents with a speed of 5 cm s^{-1}. The maximum isopycnal displacement, estimated from thermistor data, for mode 2 wave was approximately 10 to 15 m. The tripod horizontal velocity data show that the bottom layer experienced separation at least up to 0.74 mab under the mode 2 long wave, with indications of the near-bottom vortex structure.

[64] Maxima in the wave-induced bottom velocities were most likely correlated with the troughs of the wave packet, but phasing uncertainties between instrument platforms again prevent a definitive correlation at this time. The mode 2 waves were accompanied by an astounding increase in the beam-C of 2 m^{-1}. Beam-C remained high for several hours, then fell slowly. Increased fluctuating vertical velocity in the lowest layers (0.38–7 mab) persisted with the rise and initial decay of the beam-C signal (Figure 10 (bottom)).

8.6. Mode 1 Polarity Reversal

[65] The energetic storm period enabled observation of various unexpected events. In one case the ISW wave train suddenly reversed its polarity from waves of depression to waves of elevation. Before the arrival of hurricane Eduard at JD 246.5, the Sea-Soar survey revealed a stratified upper water column with $N = 0.03s^{-1}$ up to 15 m below the surface and a mean barotropic current of 15 cm s^{-1}. The influence of the hurricane on the local stratification and the currents became apparent from about JD 246.1 (see Figure 11). Owing to the very energetic environment, surface wave action, wind stress, and local currents, the subsurface stratification maximum began to migrate downward and became stronger. The position of N_{max} in its downward movement crossed the middepth of the water column at JD 246.3 when the long wave field was dominated by the mode 2 component. The N_{max} attained its lowest position at 25 mab and maximum strength at JD 246.45. Soon afterward a large mode 1 ISW of 10 m amplitude arrived. Owing to the stratification these waves had opposite polarity to that of the ISW generally observed

in the experiment. Unfortunately at the time of the arrival of the ISW of reversed polarity, the bottom tripod which collected near-bottom velocities was switched off so there is no reliable information about bottom current speeds.

[66] The ADCP current data (Figure 11) indicates that the large mode 1 ISW was propagating nearly perpendicularly to the mean current. We speculate that the local current projected onto the wave track was reversed during ISW passage, thus resulting in resuspension, perhaps due to global instability. The proximity to the bottom of the N_{max} and the large amplitude ISW conspired to cause the largest resuspension event in the experiment, increasing beam-C to the extreme value of 15 m^{-1}. The ISW of reversed polarity continued in the record until approximately JD 247.8 when the ascent of the N_{max} location again crossed the half depth of the water column.

8.7. Surface Wave Resuspension Event

[67] Although we believe that resuspension related to internal waves is dominant, surface waves cannot be neglected as agents of resuspension. Clearly, any process capable of reversing the near-bottom current over a sufficient timescale can stimulate resuspension within the context of the global instability mechanism. Thus the action of surface wave trains or surface waves which force changes in direction of the near-bottom velocity with sufficiently large magnitude and sufficiently low frequency would also satisfy the criterion for creating the required threshold conditions.

[68] The CMO 96 experiment captured such a resuspension event triggered by surface waves at JD 258.73, corresponding to a day when hurricane Hortense was passing at its closest distance of 350 km away from the mooring. The surface waves generated in response to wind stress prior to this time propagated toward the shore. At JD 258.55 the wind stress decreased and 4 hours later, the direction of propagation of the surface waves changed. This resulted in a temporary current reversal near the bottom (Figure 12). Around JD 258.73 the surface waves changed their character (possibly due to the change by nearly 180° in wind direction) and the near-bottom layer separated. The vertical extent of the separation bubble was somewhere between 1.1 to 2.2 mab. The averaged (over the surface wave period) current direction within 0 to 1.1 mab reversed, while the direction of the similarly averaged current at 2.2 mab and higher remained constant.

[69] The timescale of the current changes was commensurate with the local Brunt-Väisälä period and the near-bottom layer response was the same as forcing by a long internal wave. The near-bottom reversed current resulted in an increased beam-C up to 4 m^{-1}, which subsequently returned to its background value after 1/2 hour.

9. Concluding Remarks

[70] Several examples of resuspension stimulated by packets of long internal waves moving in a month-long record of the CMO96 experiment have been reported. These data reveal that resuspension events occur episodically and, most likely, when special threshold conditions are realized in the wave-induced boundary layer. They also reveal the possibility of existence of a long wave resonance in which energy is transferred rapidly between mode 1 and mode 2.

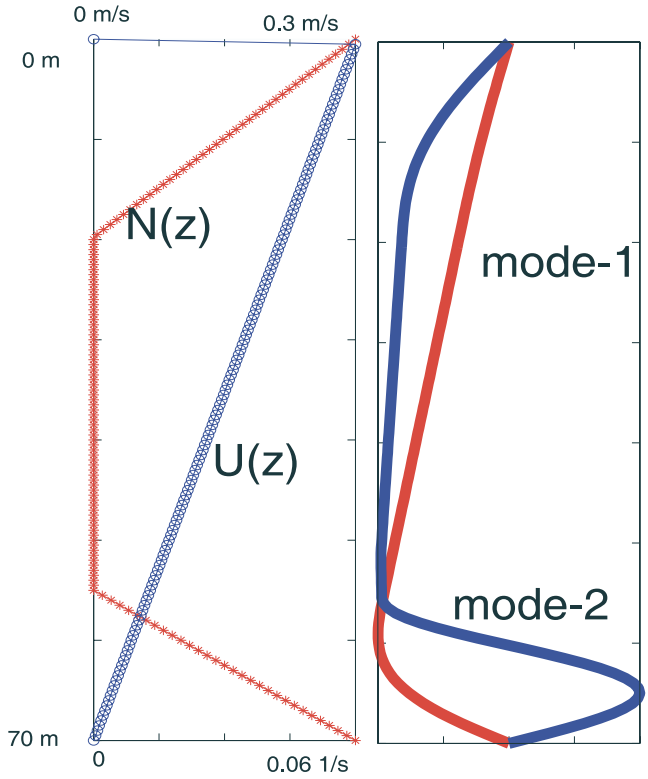

Figure A1. Mean conditions, $N(z)$ and $U(z)$, corresponding to the case from Figure 8, and associated eigenfunction calculated from equation (A1).

Numerical simulations relating to the sensitivity of this resonance in environmental conditions similar to those in this data set have been made. Results of these calculations will be reported elsewhere, but the occurrence of this type of resonance in bimodal stratifications can be expected, and the sharpness of the resonance is very sensitive to weak currents.

Appendix A: Long Internal Waves

[71] We introduce some elements of linear wave theory here to reveal the basis for our calculations of modal properties of long waves in different environments. The properties of long linear internal waves in a general waveguide are given by the Taylor-Goldstein equation (for a review see *Maslowe and Redekopp* [1980])

$$\phi'' - \frac{U''}{(U-c)}\phi + \frac{N^2}{(U-c)^2}\phi = 0 \qquad \phi(0) = \phi(h) = 0. \quad \text{(A1)}$$

This equation determines the phase speed c (eigenvalue) and modal amplitude φ (eigenfunction) for inviscid, long internal wave modes in a waveguide of depth h, where the mean flow, $U(z)$, has velocity shear. All velocities are measured relative to the stationary bottom boundary. The eigenfunction $\phi(z)$ is directly proportional to the vertical velocity and its gradient yields the perturbation horizontal velocity relative to $U(z)$. The profile of the Brunt-Väisälä frequency $N(z)$ and the velocity $U(z)$ are approximated by piecewise continuous functions and solved either analytically or

numerically. The critical layer modes (modes where $U = c$ at some intermediate depth in the waveguide) require a quite strong mean flow and we exclude them from the analysis in our calculations. Modes with critical layers can be computed [*Maslowe and Redekopp*, 1980], but they are not believed to be relevant to the cases we have analyzed. The calculations for the bottom-trapped modes are shown in Figure A1.

[72] **Acknowledgments.** We gratefully acknowledge contribution from T. Dickey (UCSB) and M. Levine (OSU) for the central mooring data and J. H. Trowbridge (WHOI) and Y. Agrawal (Sequoia) for SuperBass tripod data. The ERS-2 SAR imagery was kindly provided by R. Romeiser and W. Alpers at the Institute of Oceanography of the University of Hamburg. We thank S. Pierce (OSU) for the tidal simulations. The RADARSAT images used here were provided by the Canadian Space Agency under the Application Development and Research Opportunity Program (ADRO) project 457. We also thank anonymous reviewers for their help in improving the paper.

References

Barth, J. A., D. Bogucki, S. D. Pierce, and P. M. Kosro (1998), Secondary circulation associated with a shelf break front, *Geophys. Res. Lett.*, *25*, 2761–2764.

Bogucki, D. J., and L. G. Redekopp (1999), Global instability of separated flows: A paradigm for sediment resuspension by internal waves, *Geophys. Res. Lett.*, *26*, 1317–1320.

Bogucki, D. J., L. Redekopp, and T. Dickey (1997), Mixing by resonantly generated internal solitary waves, *J. Phys. Oceanogr.*, *27*, 1181–1196.

Boyd, T., M. Levine, and S. R. Gard (1997), SAR primer and CMO program, *Data Rep. 164*, 157 pp., Oreg. State Univ., Corvallis.

Dickey, T. D., G. C. Chang, Y. C. Agrawal, A. J. Williams III, and P. S. Hill (1998), Sediment resuspension in the wakes of hurricanes Edouard and Hortense, *Geophys. Res. Lett.*, *25*, 3533–3536.

Egbert, G. D., and R. D. Ray (2000), Significant dissipation of tidal energy in the deep ocean inferred from satellite altimeter data, *Nature*, *405*, 775–778.

Gerkema, T., and J. T. F. Zimmerman (1995), Generation of nonlinear tides and solitary waves, *J. Phys. Oceanogr.*, *25*, 1081–1094.

Gill, A. E. (1982), *Atmosphere-Ocean Dynamics*, 662 pp., Elsevier, New York.

Gottwald, G., and R. Grimshaw (1998), The formation of coherent structures in the context of blocking, *Rep. 98(3)*, Monash Univ. Dep. of Math., Melbourne.

Hammond, D. A., and L. Redekopp (1998), Local and global instability properties of separation bubbles, *Eur. J. Mech. B Fluids*, *17*, 145–164.

Hill, P. S., G. Voulgaris, and J. H. Trowbridge (2001), Controls on floc size in a continental shelf bottom boundary layer, *J. Geophys. Res.*, *106*, 9543–9549.

Huerre, P., and P. A. Monkewitz (1990), Local and global instabilities in spatially developing flows, *Annu. Rev. Fluid Mech.*, *22*, 473–537.

Lamb, K. G. (1994), Numerical experiments of internal wave generation by strong tidal flow across a finite amplitude bank edge, *J. Geophys. Res.*, *99*, 843–864.

Lentz, S., K. Shearman, S. Anderson, A. Plueddemann, and J. Edson (2003), Evolution of stratification over the New England shelf during the Coastal Mixing and Optics study, August 1996–June 1997, *J. Geophys. Res.*, *108*(C1), 3008, doi:10.1029/2001JC001121.

Maslowe, S., and L. G. Redekopp (1980), Long nonlinear waves in stratified shear flows, *J. Fluid Mech.*, *101*, 321–348.

Ostrovsky, L. A., and Y. A. Stepanyants (1989), Do internal solitons exist in the ocean?, *Rev. Geophys.*, *27*, 293–310.

Pier, B., P. Huerre, J.-M. Chomaz, and A. Couairon (1998), Steep nonlinear global modes in spatially developing media, *Phys. Fluids*, *10*, 2433–2435.

Pierce, S. D., J. A. Barth, and P. M. Kosro (1998), Acoustic Doppler current profiler observations during the CMO: Rv Endeavor cruises, *Data Rep. 169*, Oreg. State Univ., Corvallis.

Porter, D. L., D. R. Thomson, W. Alpers, and R. Romeiser (2001), Remotely sensed ocean observations of the Coastal Mixing and Optics site from synthetic aperature radars and advanced very high resolution radiometers, *J. Geophys. Res.*, *106*, 9623–9637.

Redekopp, L. G. (2002), Elements of instability for enviromental flows, in *Environmental Stratified Flows*, edited by R. H. J. Grimshaw, pp. 223–281, Springer, New York.

Shaw, W. J., J. H. Trowbridge, and A. J. Williams III (2001), Budgets of turbulent kinetic energy and scalar variance in the continental shelf bottom boundary layer, *J. Geophys. Res.*, *106*, 9551–9564.

Stastna, M., and K. G. Lamb (2002), Vortex shedding and sediment resuspension associated with the interaction of an internal solitary wave and the bottom boundary layer, *Geophys. Res. Lett.*, *29*(11), 1512, doi:10.1029/2001GL014070.

Wang, B., and L. G. Redekopp (2001), Long internal waves in shear flows: Topographic resonance and wave-induced global instability, *Dyn. Atmos. Oceans*, *33*, 263–302.

Wang, B.-J., D. J. Bogucki, and L. G. Redekopp (2001), Internal solitary waves in a structured thermocline with implications for resuspension and the formation of thin particle-laden layers, *J. Geophys. Res.*, *106*, 9565–9585.

J. Barth, College of Oceanic and Atmospheric Sciences, Oregon State University, 104 COAS Administration Building, Corvallis, OR 97331-5503, USA. (barth@coas.oregonstate.edu)

D. J. Bogucki, Rosenstiel School of Marine and Atmospheric Science, University of Miami, 4600 Rickenbacker Causeway, Miami, FL 33149, USA. (dbogucki@rsmas.miami.edu)

L. G. Redekopp, Department of Aerospace and Mechanical Engineering, University of Southern California, 3650 McClintock Avenue OHE 430, Los Angeles, CA 90089-1453, USA. (redekopp@spock.usc.edu)